

EFFECT OF ANNEALING BELOW α -TRANSUS TEMPERATURE ON THE MICROSTRUCTURAL EVOLUTION OF Ti-46Al-2Nb-2Mn

*A Thesis Submitted in Partial Fulfillment
of the Requirements for the
Degree of Master of Technology*

by

SOMA PRASAD

to the

**Department of Materials and Metallurgical Engineering
Indian Institute of Technology, Kanpur**

February, 2000

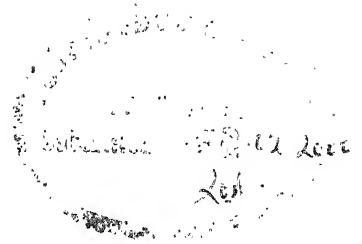
15 MAY 2000/MME
CENTRAL LIBRARY
I. I. T., KANPUR
A 130852

Th
MME/2000/M
P886c



A130852

CERTIFICATE



This is to certify that the work contained in this thesis entitled **“Effect of annealing below α -transus temperature on the microstructural evolution of Ti-46Al-2Nb-2Mn”** has been carried out by **Ms. Soma Prasad** under my supervision and that this work has not been submitted elsewhere for a degree.

A handwritten signature in black ink, appearing to read "Sandeep Sangal".

(Dr. Sandeep Sangal)

Associate Professor

Department of Materials and Metallurgical Engineering

Indian Institute of Technology, Kanpur

ACKNOWLEDGEMENT

I wish to acknowledge my heartfelt gratitude and immense indebtedness to my guide, **Dr.S.Sangal**, professor, Department of Materials and Metallurgical Engineering, IIT Kanpur, for his valuable suggestions and motivation during the different phases of investigation and preparation of the thesis.

I take this opportunity to thank all my teachers of the Department of Materials and Metallurgical Engineering, IIT Kanpur, for sharing their knowledge with me.

I would also like to thank Mr. H.C.Srivastav and Mr. V. Kumar who helped me immensely in carrying out the experimental work. I also acknowledge Mr. Prasad and Mr. Rahman for their cooperation. My sincere thanks are due to Mr. Uma Shankar, Mr.R.P.Singh, Mr.U.S.Lal, Mr.Sharma, Mr.Agnihotri and Mr. B.K.Jain for their help and cooperation during various stages of work.

I would like to extend my special thanks to all my friends at IIT Kanpur whose consistent affection and encouragement made my stay at Kanpur a memorable one.

Finally, I greatly acknowledge the inspiration and moral support of my parents and my sisters in all my endeavors.

SOMA PRASAD

CONTENTS

CERTIFICATE	i
ACKNOWLEDGEMENT	ii
LIST OF TABLES	v
LIST OF FIGURES	vi
ABSTRACT	viii
CHAPTER	PAGE
1. INTRODUCTION	1-3
2. LITERATURE REVIEW	4-24
2.1 Ti-Al binary phase diagram	4
2.2 Structure of phases	5
2.2.1 Ti_3Al	
2.2.2 $TiAl$	
2.3 Effect of alloying additions	7
2.4 Deformation behaviour and mechanical properties	8
2.4.1 Ti_3Al	
2.4.2 $TiAl$	
2.5 Oxidation resistance	10
2.6 Effect of hydrogen environment	10
2.7 Phase transformation	11
2.7.1 Lamellar structure	
2.7.2 Discontinuous coarsening	
2.7.3 Massive transformation	
2.7.4 Ordering reaction	
2.8 Microstructural evolution	17

2.9	Processing and microstructural control	18
2.10	Microstructure/ Mechanical property relationship	19
2.11	Applications	24
3.	EXPERIMENTAL PROCEDURE	25-28
3.1	Preparation of starting material	25
3.2	Heat treatments	26
3.3	Characterization of samples	26
3.3.1	Scanning electron microscopy	
3.3.2	X-Ray diffraction	
3.3.3	Electron probe micro analyser	
3.4	Microhardness test	28
4.	RESULTS AND DISCUSSION	29-51
4.1	Starting material	29
4.1.1	X-Ray diffraction	
4.2	Water quenched samples	34
4.2.1	Scanning electron microscopy	
4.2.2	X-Ray diffraction	
4.3	Furnace cooled samples	44
4.3.1	Scanning electron microscopy	
4.3.2	X-Ray diffraction	
4.4	Air cooled sample	50
4.5	Microhardness test	50
5.	CONCLUSIONS	52
	REFERENCES	54
	APPENDIX	57

List of Tables

S.No.	Page
2.1 Invariant reactions occurring in Ti-Al system.	5
4.1 EPMA result.	30
4.2 Important peaks and their relative intensities for starting material.	33
4.3 Relative intensities of important peaks for water quenched samples.	41
4.4 Volume fractions of TiAl and Ti ₃ Al phases during different heat treatment.	43
4.5 Relative intensities of important peaks for the furnace cooled samples.	49
4.6 Hardness variation during different heat treatments.	51

List of Figures

S.No	Page
2.1 (a) Ti-Al binary phase diagram showing various phases.	
(b) Part of binary Ti-Al phase diagram in the region of interest.	6
2.2 (a) and (b) Unit cell of TiAl and Ti ₃ Al.	7
2.3 CCT diagram showing ordering reaction for (a) Ti-40Al and (b) Ti-42Al.	16
2.4 Flow chart showing various processing routes practiced for gamma alloys.	20
2.5 Effect of grain size on tensile strength.	21
2.6 Comparison of creep properties of different types of microstructures.	23
2.7 Comparison of fatigue properties.	23
4.1 (a) and (b) SEM micrographs of the as-received material at different magnification.	31
4.2 SEM micrographs of the starting material at, (a) 300X showing large grains, (b) 1200X showing serrated boundary and (c) 5000X showing fine details.	31
4.3 (a) and (b) XRD patterns from the starting material in two different orientations.	32
4.4 SEM micrographs of the water quenched samples from, (a) 850 ⁰ C, (b) 900 ⁰ C, (c) 1150 ⁰ C and (d) 1320 ⁰ C.	36
4.5 XRD patterns from the water quenched samples from, (a) 1320 ⁰ C, (b) 1150 ⁰ C, (c) 900 ⁰ C.	38
4.5 SEM micrographs of the furnace cooled samples at different magnifications from, (a) and (b) 900 ⁰ C, (c) and (d) 1150 ⁰ C.	45

4.7	SEM micrograph of sample furnace cooled from 1200 ⁰ C.	46
4.8	XRD patterns from the samples furnace cooled from, (a) 1150 ⁰ C and (b) 900 ⁰ C.	47
4.9	SEM micrograph of the sample air cooled from 1150 ⁰ C.	50

ABSTRACT

Two phase gamma based titanium aluminide of composition Ti-46Al-2Nb-2Mn was used in the present investigation to study effect of annealing below α -transus temperature on the microstructural evolution. In order to achieve this, the samples were homogenized prior to all the heat treatments by ice water quenching from 1400°C. Heat treatments were done at 850°C, 900°C, 1150°C, 1200°C and 1320°C for various holding times followed by water quenching, air cooling and furnace cooling. The heat treated samples were characterized using scanning electron microscopy, X-ray diffraction and electron probe micro analyser. X-ray diffraction results were used to determine volume fraction of the phases. Microhardness of samples was also measured to study the effect of microstructure on hardness of the material.

In this material, four types of microstructure are generally observed, these are, fully lamellar, nearly lamellar, duplex and near gamma. In the present investigation, fully lamellar structure was obtained at 850°C. Continuous as well as discontinuous coarsening was observed in sample water quenched from 1150°C while monolithic γ structure was observed on furnace cooling from 900°C and 1150°C. Extent of discontinuous coarsening was observed to be maximum at 1320°C. Hardness of the material decreases as monolithic γ structure is formed and hardness decreases as the extent of coarsening increases in the material. Volume fractions of the phases, as obtained from the XRD showed very good agreement with the volume fractions obtained from phase diagram though some discrepancy was observed in water quenched samples which might be due to some transformation that may have occurred during quenching.

CHAPTER 1

INTRODUCTION

High temperature materials operate under severe conditions hence, ideal materials for high temperature moving components should have a combination of high melting point, low density, good elevated temperature strength and stiffness, good room temperature ductility, superior creep properties and appreciable oxidation and corrosion resistance. Over past few decades, nickel, titanium and aluminum based intermetallics are being considered as potential candidates for high temperature applications over the conventional alloys because of their high melting point, low density and high temperature strength.

The ordered intermetallics show appreciable increase in high temperature strength by offering activation barrier to the flow process required for deformation as a result of high energy bonds between the unlike atoms. However, the resistance to material flow due to long range ordering renders them extremely brittle at ambient temperatures which is the major impediment to its wide applicability.

Gamma based titanium aluminides have attracted a great deal of attention from the aerospace community and the automobile industry because of their much lower density

than the superalloys alongwith good creep properties, good oxidation and burn resistance and high temperature strength retention. Among the gamma titanium aluminides, only two phase alloys are of engineering potential since they exhibit better combined mechanical properties than those of single phase gamma alloys.

The gamma based titanium aluminides are very sensitive to alloy chemistry, microstructure and thermomechanical processing. Small additions of vanadium, chromium and manganese increase the ductility of two phase gamma alloys. Addition of boron and tungsten modifies the fully lamellar structure while silicon and carbon enhances creep resistance. Niobium and tantalum are added to improve oxidation resistance of the material. Heat treatment prior to and after hot working remains the most potent method of altering the mechanical properties.

For the development of an alloy, a thorough understanding of the Processing-Microstructure-Property relationship for the system is essential. Due to complexity of the phase diagram, numerous transformation modes appear during various heat treatments. They are, formation of two phase lamellar structure, ordering reaction, massive type transformation, discontinuous coarsening of the lamellar structure and formation of monolithic gamma grains. However, complete understanding of the phase transformation and mechanism operative during these transformations has not yet been achieved.

An attempt is made in the present investigation to get some understanding about the transformation modes occurring during different heat treatments. The overall objective of

this investigation is to develop an understanding of the effect of annealing temperature (below α -transus temperature) and cooling rates on the evolution of microstructure. The specific tasks required to achieve this objective are to obtain correlation between coarsening behaviour, annealing temperature and holding time, cooling rates, volume fraction of different phases and hardness of the material.

CHAPTER 2

LITERATURE REVIEW

The Ti-Al alloy system has been of interest since titanium first became commercially available half a century ago. To study the salient features of the alloy, it requires knowledge of phase equilibria and transformations and also effect of alloying additions. Hence it is necessary to throw some light on the Ti-Al binary phase diagram.

2.1 Ti-Al Binary Phase Diagram

Presence of interstitial elements like oxygen and hydrogen in the range 1000-2000ppm and also inability of light microscopy to distinguish α from α_2 and the presence of short range order in the α phase at aluminum content below the $\alpha/\alpha + \alpha_2$ boundary, hampered the determination of boundary positions for long.

According to the binary phase diagram proposed by Murray [1], the β and α_2 fields are separated by a narrow α field. He also proposed that α decomposes to $\alpha_2 + \gamma$ by eutectoid reaction. But this diagram imposes a restriction that the α phase is in equilibrium with

solid phases only. This phase diagram was further modified by Mc Cullough et al [1]. He introduced two peritectic reactions, $L + \beta \rightarrow \alpha$ and $\alpha + L \rightarrow \gamma$. It was also suggested that eutectoid reaction is virtually impossible because of the large difference in the kinetics of the two products α_2 and γ . Figure 2.1 shows a recent version of the binary phase diagram. Important invariant reactions are summarized in table 2.1.

Table 2.1: Invariant Reactions in Ti-Al system

Reaction	Nature	Temperature($^{\circ}\text{C}$)
$L + \beta \rightarrow \alpha$	Peritectic	1490
$L + \alpha \rightarrow \gamma$	Peritectic	1460
$\alpha \rightarrow \alpha_2 + \gamma$	Eutectoid	1118

2.2 Structure of Phases

2.2.1 $\text{Ti}_3\text{Al}(\alpha_2)$

This phase exhibits non stoichiometry and undergoes an order-disorder transformation in the range of 22 to 39% Al and congruently at 1180 $^{\circ}\text{C}$. Ti_3Al has hexagonal (DO_{19}) structure (Ni_3Sn type) with $a = 5.782 \text{ \AA}$ and $c = 4.629 \text{ \AA}$. c/a ratio is 0.8. Figure 2.2a shows the structure of Ti_3Al .

2.2.2 $\text{TiAl}(\gamma)$

TiAl or the γ phase crystallizes as tetragonal L1_0 structure (AuCu type). The L1_0 structure results due to ordering in the fcc lattice(Al). The face centered cubic structure is

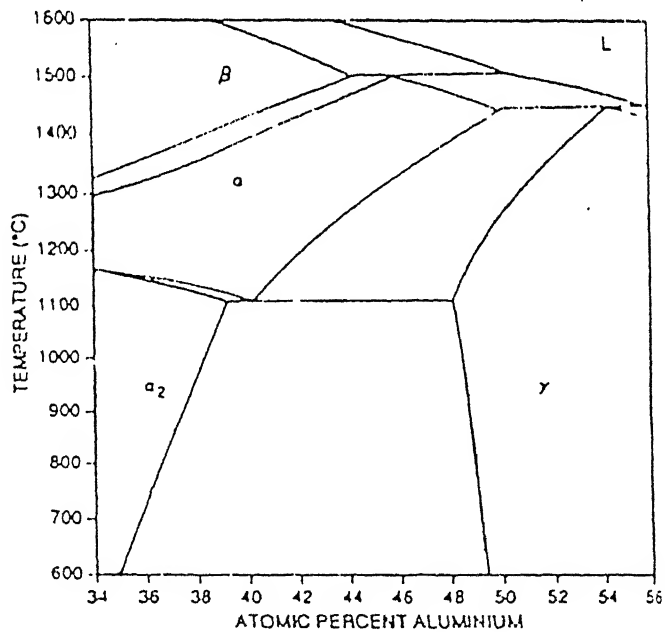
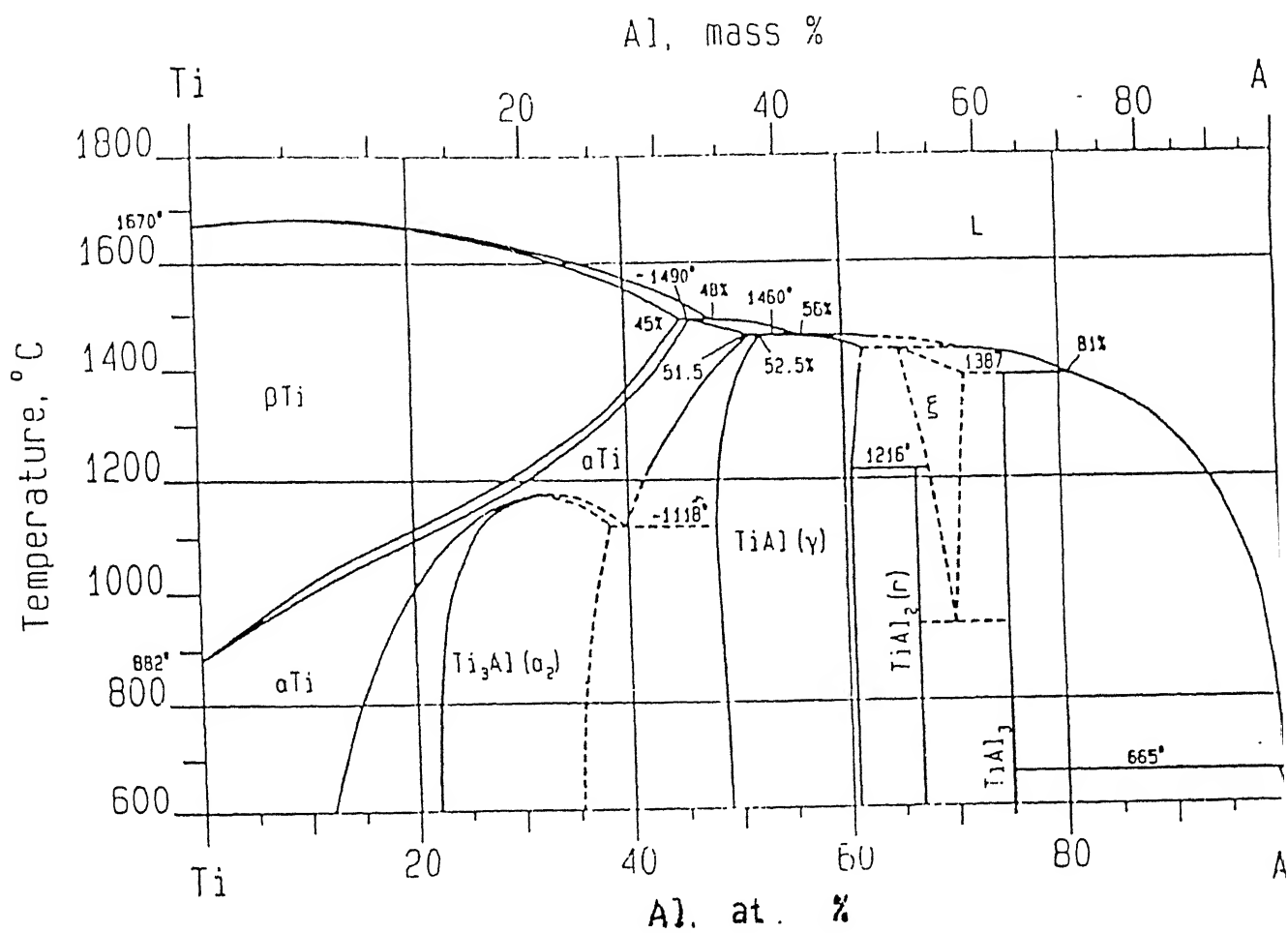


Figure 2.1: (a) Ti-Al binary phase diagram showing various phases, (b) Part of binary Ti-Al phase diagram in the region of interest.

tetragonally distorted because alternate (002) planes are occupied by the atoms of the same component. This ordered structure is stable upto the melting temperature of γ . The lattice parameters are $a = 4.005 \text{ \AA}$ and $c = 4.07 \text{ \AA}$ with tetragonality of 1.02. Figure 2.2b shows the structure of TiAl.

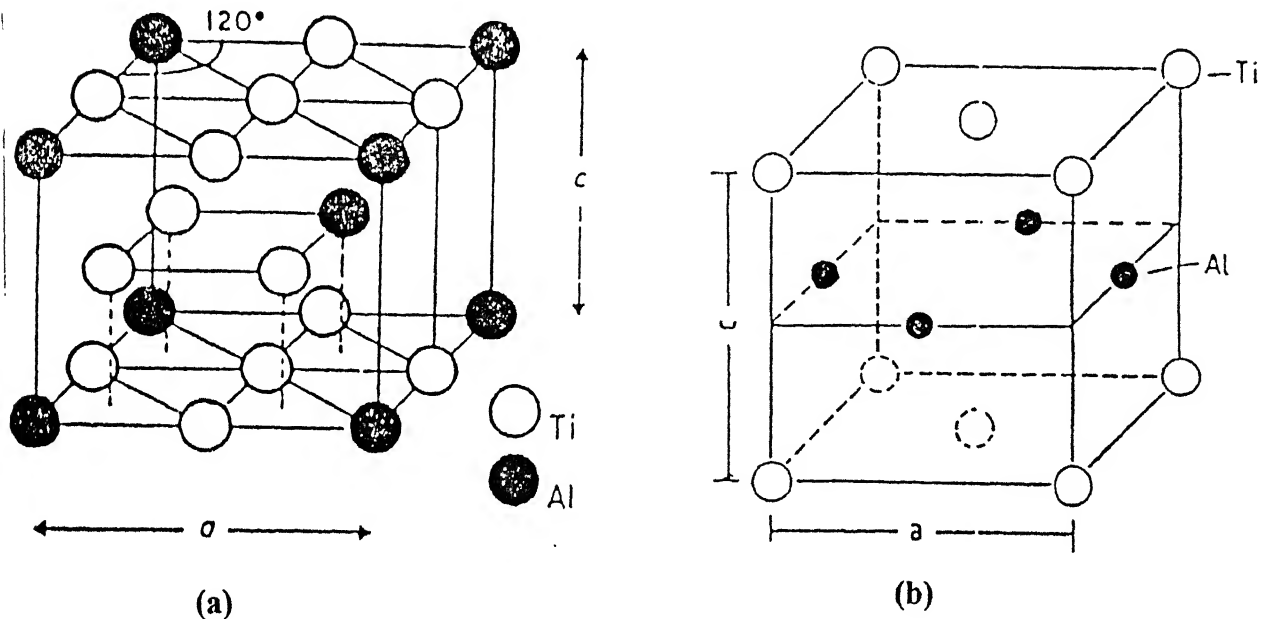


Figure 2.2: Unit cell of (a) Ti₃Al and (b) TiAl

2.3 Effect of Alloying Additions

Addition of Nb in α_2 alloys helps in improving almost all the material properties except creep resistance since Nb substitutes for Ti atoms and increases the number of slip systems. Other alloying additions are Mo, Ta, Cr for improving strength, Mo for creep resistance and Ta, Mo to improve oxidation resistance. Improvement in elevated temperature strength, creep resistance and environment is in general favoured by β -stabilizer addition, high Al content and low vanadium.

The γ based alloys, most commonly used have composition of Ti-(46-52)Al-(1-10)M where M is atleast one element from V, Cr, Mn, Nb, Ta, W, and Mo. These alloys can be divided into single phase(γ) or two phase ($\gamma + \alpha_2$) alloys. Single phase alloys contain third alloying element such as Nb or Ta that promotes strengthening and enhances oxidation resistance. In two phase alloys, alloying elements V, Cr, Mn is added to raise ductility and Nb, Ta for better oxidation resistance.

2.4 Deformation Behaviour and Mechanical Properties

2.4.1 Ti₃Al

Low temperature ductility of Ti₃Al based alloys can be attributed to the planarity of slip and absence of slip in planes parallel or inclined to hexagonal axis. An important difference in the deformation behaviour of Ti₃Al and other hcp metals and alloys is the absence of twinning. The long range order suppresses twinning in Ti₃Al because such deformation produces disorder and hence slip is preferred.

The mechanical properties of monolithic α_2 alloys depend on composition and the microstructure developed by thermomechanical processing. The fracture behaviour depends on the presence of β /B2 phase and also on the slip behaviour of α_2 . The tensile properties of Ti₃Al-Nb alloys are related to shape, volume fraction and distribution of the α_2 and B2 phases, with boundary strengthening playing important role. Room temperature ductility can be dramatically improved by producing optimum amount of

equiaxed α_2 grains. Alloys with widmanstatten α plates show low elevated temperature low cycle fatigue. The charpy impact strength is extremely low. Creep resistance can be enhanced with colony type microstructure.

2.4.2 TiAl

TiAl has lower density, higher strength and better oxidation resistance than α_2 . The deformation behaviour of γ alloys is anisotropic. The $L1_0$ alloys show an anomalous in flow stress as temperature increases. The deformation modes in the TiAl based alloys depends on the Al content, i.e, presence of α_2 phase. Although γ based alloys have higher elastic modulus, lower density and better elevated properties than α_2 alloys, the room temperature ductility and fracture resistance is poor. Addition of 1-3% V, Mn and Cr enhances the ductility while Nb, Ta and Mn are added to improve strength and oxidation resistance. The Ti-52Al alloy demonstrates the lowest hardness value at room temperature, independent of thermomechanical treatment. At 1000°C, the strength gradually decreases with increase in Al content. The nano structure region of microstructure scale can increase ductility and at the same time decrease the ductile-brittle transition temperature by about 200°C. The fine grain also raises the fatigue life at temperatures below 800°C. Both fracture toughness and impact resistance are low at ambient temperature. However fracture toughness increases with increasing temperature and with high proportions of lamellar structure. High Al content and W additions increase the creep resistance considerably. Increase in grain size also improves the creep properties of two phase alloys. Creep can also be improved by increasing the volume fraction of lamellar structure but that decreases ductility.

2.5 Oxidation Resistance

Ti₃Al forms three zones of oxide layer. The scales consists of alternate layer of TiO₂ and Al₂O₃. At high temperatures, the oxidation kinetics tend to be dominated by TiO₂ formation hence oxidation resistance is poor. At lower temperatures more aluminum is present and an adherent alumina scale forms which restricts diffusion of oxygen. Addition of Nb improves the oxidation resistance.

TiAl has poor resistance to oxidation at temperatures above 800⁰C because above this temperature, the external layer of protective Al₂O₃ is replaced by TiO₂ layer. The crystal growth of randomly oriented grains of TiO₂ leads to the formation of numerous voids and pores at the grain boundary that leads to crack initiation and spallation of oxide films from the alloy substrate. Nb, W and Mo improve the oxidation resistance. Phosphorus is also reported to decrease the oxidation rate significantly [2]. Silicon decreases the oxidation rate by forming SiO₂ layer which is more protective than TiO₂ and Y improves the adhesion of surface oxide [3].

2.6 Effect of Hydrogen Environment

Hydrogen can strongly and adversely effect the mechanical properties of titanium based materials by reducing strain to failure, causing a brittle intergranular failure mode.

Fracture is primarily related to hydride formation as it occurs with 23% increase in volume.

Almost all hydrogen in a precharged α_2 exists as hydrides because the terminal solubility of hydrogen in this alloy is very low at room temperature. As the amount of hydride increases in these alloys, strength also increases while ductility and fracture toughness decreases. The α_2 is very susceptible to hydrogen embrittlement, either due to lattice bond interaction or as a result of localized, strain induced hydride formation in front of the crack tip, which decomposes after fracture.

Hydride formation has not been detected in TiAl exposed to high pressure hydrogen at temperature 982°C [4]. Tensile strength decreases in near γ alloy. High temperature hydrogen exposure has no effect on fracture toughness.

2.7 Phase Transformation

To understand the phase transformation, the binary phase diagram proposed by McCullough has been considered. Due to the complexity of the phase diagram for the chemical composition range of TiAl based alloys, numerous transformation modes appear during various heat treatments; formation of γ/α_2 lamellar structure, $\alpha \rightarrow \alpha_2$ ordering reaction, massive type transformation, discontinuous coarsening of the lamellar structure and formation of monolithic γ grains.

2.7.1 Lamellar Structure

Cooling results in decomposition of the α phase into a lamellar structure that is characterized by several plates of γ alternating with single α_2 lamellae. The two phases have the following relationship; $(0001)_{\alpha_2} // \{111\}_{\gamma}$ and $\langle 1120 \rangle_{\alpha_2} // \langle 110 \rangle_{\gamma}$ [5].

The mechanism of lamellar structure formation consists of different stages i.e, first the crystal structure change from hcp to fcc, then a chemical composition change through atom transfer and finally, formation of $L1_0$ γ phase by ordering. It has been established that the formation of lamellar structure does not occur through eutectoid reaction but results from the precipitation of γ lamellae in either ordered or disordered matrix i.e , by either of two routes; $\alpha \rightarrow \alpha_2 \rightarrow \gamma + \alpha_2$ or by $\alpha \rightarrow \alpha + \gamma \rightarrow \gamma + \alpha_2$. γ starts to precipitate from α or α_2 by propagation of Shockley partial dislocation. This mechanism was proposed by Blackburn [5]. According to his theory a perfect $a/3\langle 1120 \rangle$ dislocation dissociates to two Shockley partials ($a/3\langle 1010 \rangle + a/3\langle 0110 \rangle$) bordering. Such a stacking fault locally creates an fcc type stacking sequence in hexagonal matrix. Repeating this mechanism every two basal planes leads to change in crystal structure. The free energy associated with the transformation provides the driving force for separating the Shockley partials. This corresponds to the pre nucleation stage.

During nucleation stage, equilibrium γ phase is formed involving both chemical composition changes by atom transfer and the ordering of the fcc zone. Ordering process assumes existence of metastable lamellar fcc phase and during ordering, the orientation

variants nucleates at a number of separate sites in the metastable phase, followed by independent growth of the variant.

2.7.2 Discontinuous Coarsening

Primary lamellar structure modifies basically through either discontinuous coarsening or formation of monolithic γ grains. Alloy composition dictates the route selected for modification. However, monolithic γ grains form from growth of the pre-existing γ phase related to interdendritic segregation during solidification rather than to a normal coarsening of primary γ lamellae. Discontinuous coarsening is the major coarsening process of the primary lamellar structure.

Microstructural Aspects

Discontinuous coarsening of the primary lamellar structure occurs behind the migrating α or α_2 grain boundary. The resulting secondary γ lamellae remain inside the initial grain of the primary lamellar structure and they are almost parallel to the primary γ lamellae. The secondary lamellae are much coarser and the boundary between the two phases, i.e. α_2 and γ are somewhat irregular. Discontinuous coarsening develops at both sides of the grain boundary. Occurrence of serrated grain boundary is considered as an early stage of discontinuous coarsening. As the temperature of heat treatment in the $\alpha + \gamma$ phase field increases, discontinuous coarsening becomes less pronounced and tends to disappear.

Mechanism

Presence of planar, extremely flat and highly coherent interfaces between the two phases in the primary lamellar structure makes normal coarsening extremely difficult. However, a discontinuous reaction can occur at grain boundary with sufficient mobility so that the primary γ lamellae of the adjacent grain dissolves at the moving grain boundary front and reprecipitate behind it. The migrating grain boundaries tend to become sinuous during discontinuous coarsening while the grain size remains the same, hence there is increase in the total grain boundary energy. This increase is compensated by reducing the number of interface between the two phases hence formation of coarser lamellae. Yamabe et al [6] showed that the extent of discontinuous coarsening is higher for finer primary lamellar structure.

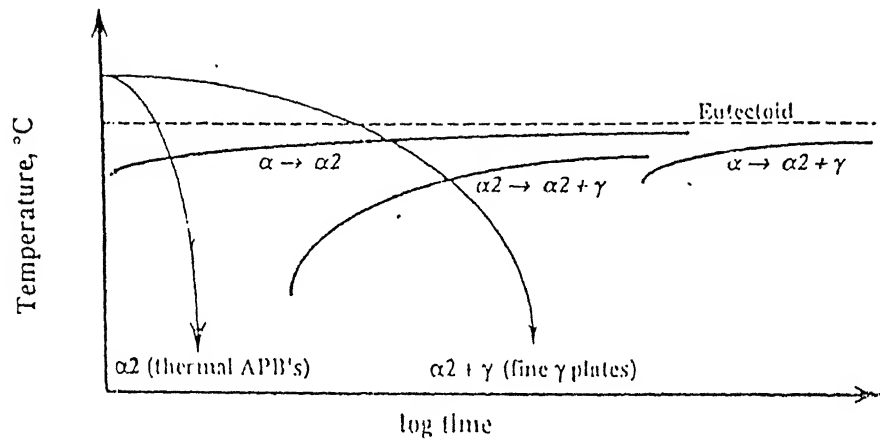
2.7.3 Massive Transformation

During rapid cooling from the single α phase field, a massive type transformation with direct transition of α to γ replaces the primary γ precipitation. This transformation is characterized by feathery γ_m grains often in presence of dispersed, fine lamellar colonies formed from retained α . The massively transformed γ phase, γ_m , is constituted of a large number of faulted domains and the boundary between them do not lie along any particular crystallographic plane. γ_m shows no orientation relationship with the disordered α matrix parent phase into which it grows. This transformation mechanism is generally operative in alloys having near stoichiometric composition.

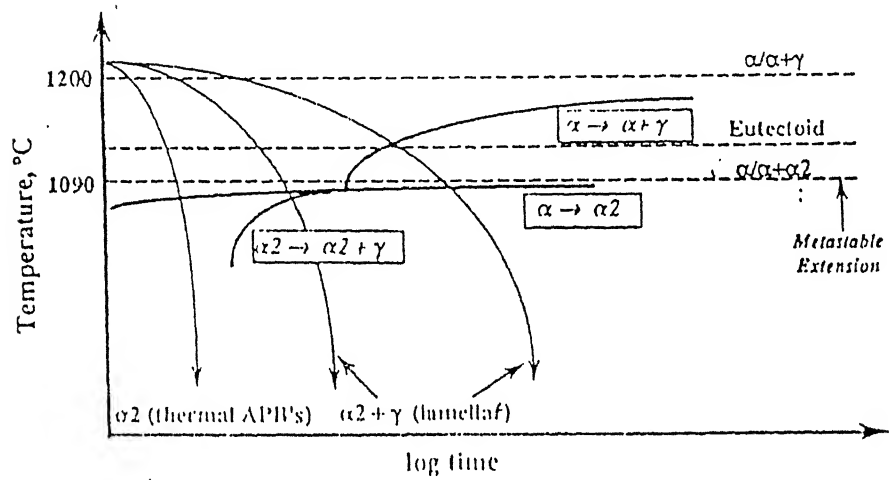
The mechanism involved in the massive transformation has been studied in details by Zhang et al [7] and Denquin and Naka [6]. It has been proposed that upon quenching, the α phase becomes unstable and begins to decompose to lamellar γ by Blackburn mechanism. This γ develops preferentially in the vicinity of grain boundaries that can supply the necessary Shockley partial dislocations and associated stacking faults. The γ nuclei form coherent interface with one grain and tend to grow into the neighbouring grain. The interface between the growing γ and the grain into which it is growing is incoherent which favours the transfer of atoms across the interface and hence growth. The γ_m nuclei most likely grow by a mechanism involving thermally activated short range jumps of atoms across the incoherent α/γ interfaces. Transformation induced stress concentration is relieved by twinning, resulting in twin and pseudo twin related domains within the γ_m . Addition of Nb retards lamellar transformation and thereby promotes both massive and martensitic transformations.

2.7.4 Ordering Reaction

The $\alpha \rightarrow \alpha_2$ transformation is simple ordering reaction. The reaction involves ordering of a disordered hexagonal structure. Consequently, the transformation from α to α_2 can occur quickly and without any significant undercooling. This transformation is dictated by composition and cooling rate. The CCT diagram reproduced in figure 2.3 [8] shows that transformation of α to α_2 cannot be suppressed even by rapid quenching for aluminum contents between 40-45 at%.



(a)



(b)

Figure 2.3: CCT diagram showing ordering reaction for (a) Ti-40Al and (b) Ti-42Al.

2.8 Microstructural Evolution

A comprehensive study of microstructural development in two phase TiAl was carried out by Kim [9]. According to him four types of structures are obtainable through various heat treatments. They are fully lamellar, nearly lamellar, duplex and near gamma.

The alloys containing less than 48 at% Al forms nearly lamellar structure for heat treatment at temperatures close to α -transus. This structure consists of primarily coarse lamellar structure with small amounts of γ grains. Heat treatments at temperature above α -transus results in fully lamellar microstructure consisting of alternate layers of γ and α_2 plates. Lamellar structure forms as a result of nucleation of γ plates in α or α_2 matrix. This may take place by either of the two routes; $\alpha \rightarrow \alpha_2 \rightarrow \gamma + \alpha_2$ or $\alpha \rightarrow \alpha + \gamma \rightarrow \gamma + \alpha_2$

The near gamma microstructure consists of entirely gamma grains in single phase alloys or predominantly gamma grains with finely dispersed grain boundary α_2 particles in two phase alloys. The alloys containing more than 52 at% Al lie in the single phase γ field over the entire temperature range. Duplex microstructure is produced after annealing treatments in the $\alpha+\gamma$ phase field at temperatures where the α and γ phases are approximately equal in volume. It consists of equal volumes of equiaxed γ grains and $\alpha+\gamma$ lamellar grains.

2.9 Processing and Microstructural Control

The γ -based alloys are processed by conventional methods including casting, ingot metallurgy, powder metallurgy, sheet forming methods and also by novel means like rapid solidification (splat cooling, melt spinning and laser heating) and mechanical alloying. Important alloying/melting processes include induction skull melting, vacuum arc remelting and plasma arc melting.

The cast ingot microstructures are normally fully lamellar with occasional shrinkage pores and a small amount of pro-eutectoid γ phase which is removed by Hot Isostatic Pressing (HIPing). However, this approach results in large grains and hence inferior properties. Hot working is done near the eutectoid temperature (approx. 1200 °C) [10] in case of forging or at higher temperatures for extrusion. Forging results in banded structure consisting of a fine, partially recrystallized γ grain matrix dispersed with fine α_2 particles and some original lamellar grains. Extrusion done near eutectoid temperature also results in similar structure but less homogenous. Extrusion at higher temperature yields fine duplex structure.

The processed products are given two step heat treatment. In the first step, the hot worked material is solutionized in α or $\alpha+\gamma$ phase field to control the lamellar/ γ grain volume ratio. Second step heat treatment is done to stabilize the microstructure and phase compositions by treatment in $\alpha_2+\gamma$ phase field.

Microstructures obtained in hot worked material formed by PM routes are much more fine and homogenous than the ingot casting route microstructure. However they lack sufficient creep resistance and crack growth resistance. Rapid Solidification processing of titanium aluminides offer the potential of improved ductility by disordering and grain refinement.

Flow chart in figure 2.4 shows various processing methods and routes practiced for engineering gamma alloys.

2.10 Microstructure/Mechanical Property Relationship

Microstructure has a strong effect on almost all the mechanical properties including tensile properties, fracture toughness, creep and fatigue properties.

The room temperature elongation of gamma alloys ranges from 0.3-0.4%, and yield and tensile strengths vary from 250-600Mpa and 300-700Mpa respectively. The fully lamellar microstructure exhibits lower strength than the duplex structure. Tensile strength increases with decrease in grain size. A strong effect of grain size in fully lamellar structure is also observed on the tensile strength which is shown in figure 2.5 [11]. Variation of strength with temperature is also a function of microstructure with fully lamellar structure exhibiting better high temperature strength retention. The duplex alloys containing 45-50 at% Al shows appreciable ductility and it is maximum for duplex alloys

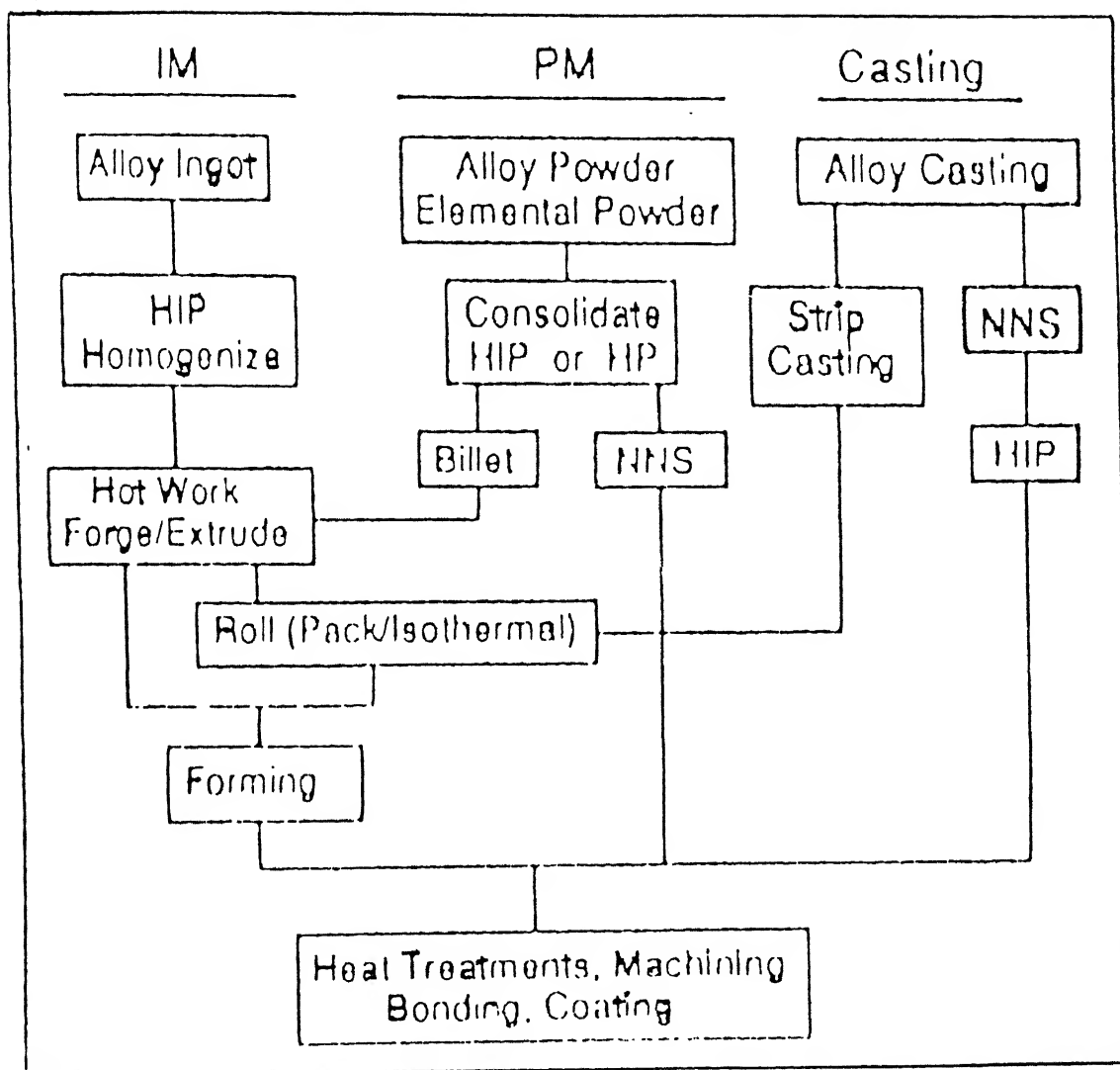


Figure 2.4: Flow chart showing various processing routes practiced for gamma alloys.

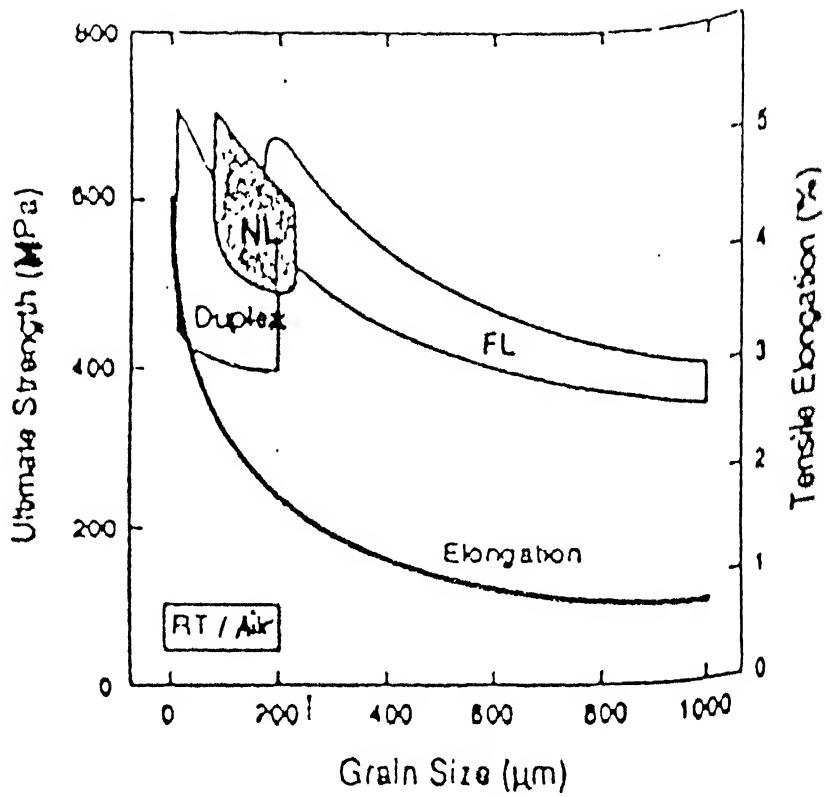


Figure 2.5: Effect of grain size on tensile strength.

with 48 at% Al[11,12]. However, highest ductility is obtained for fine grained duplex structure with uniform grain sizes and fracture strains ranging from 2-4%.

The fully lamellar structure exhibits poor tensile properties which can be attributed to large grain size, lack of slip/twinning activity and low cleavage stresses[13,14]. However, alloys with fully lamellar structure exhibit high fracture toughness ranging from 25-30MPa(m)^{1/2} as compared to 15-20MPa(m)^{1/2} of alloys with duplex structure. The single γ phase alloys exhibit the lowest fracture toughness of $\sim 10\text{MPa(m)}^{1/2}$ [11]. The fracture toughness of the lamellar structure depends on the orientation of the lamellae relative to the crack plane. Highest toughness value is obtained if crack traverses across the lamellae than when it does along the lamellar interface.

Increase in Al content in two phase alloys, grain size in single phase alloys and lamellar volume fraction effectively improves creep properties. Creep resistance of fully lamellar γ based alloys is better than duplex or nearly lamellar alloys. This is shown in figure 2.6. Creep resistance in fully lamellar structures is increased by serrated grain boundaries and by refined lamellar spacing. It has been shown that grain size has no significant on creep resistance.

Duplex microstructures exhibit longer low cycle fatigue life than fully lamellar microstructure below 850°C [11]. For high cycle fatigue, duplex microstructures show better fatigue properties at lower temperatures but fully lamellar structure exhibits longer lives at high temperature. This is shown in figure 2.7. Fatigue behaviour of fully lamellar

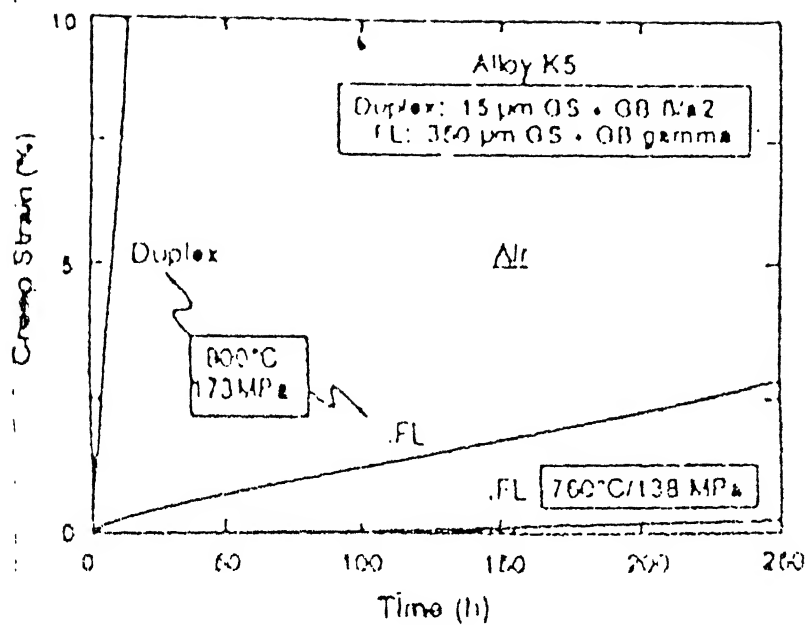


Figure 2.6: Comparison of creep properties of different types of microstructures.

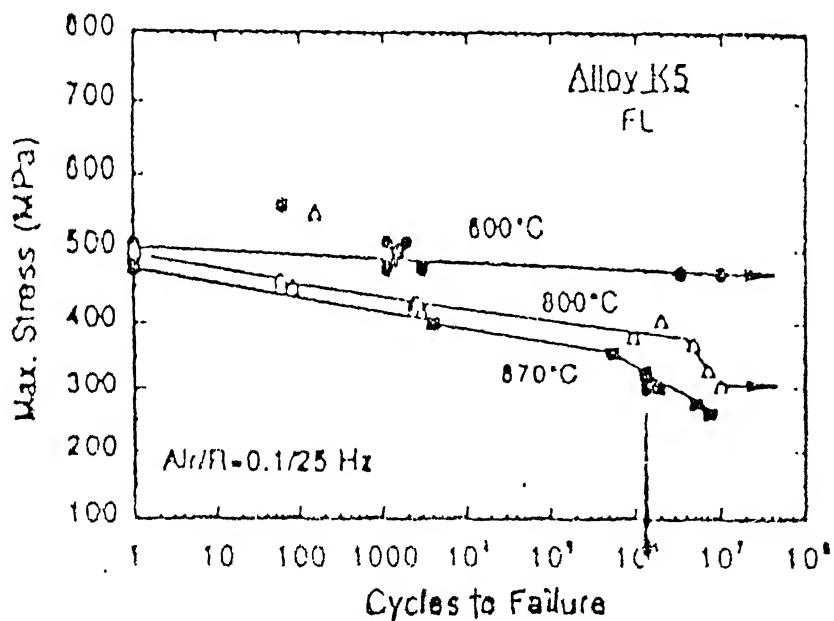


Figure 2.7: Comparison of fatigue properties.

is a function of interlamellar spacing. Crack initiation usually takes place at the specimen surface for duplex material and in the interior for fully lamellar. Microstructural inhomogeneity degrades the fatigue property.

2.11 Applications

Titanium aluminides have been recognized as potential material for significant weight reduction in jet engines and Ti-48Al-2Cr-2Nb has emerged as the first alloy to enter commercial jet engine service.

Gamma alloys are now replacing the conventional nickel based alloys in low pressure turbine blades, high pressure compressor blades, blade cover plates and stationary parts such as transition duct beams, vanes, high pressure turbine casings, swirlers, nozzles, flaps and tiles. Cast TiAl rotors are used for automotive turbochargers.

Both monolithic and composite titanium aluminides are seriously being considered for trans atmospheric vehicles such as The National Aerospace Plane (NASP). This type of applications includes skin surfaces, internal structural parts, rocket nozzles and engine parts. The attractive high temperature behaviour and low density makes monolithic and composite titanium aluminides an alternative for superalloys in many elevated temperature terrestrial, airframe, engine and missile application.

CHAPTER 3

EXPERIMENTAL PROCEDURE

The material used in the present study was procured from Rolls Royce Co., England. It has a nominal composition of Ti-46Al-2Nb-2Mn. The as received material was previously plasma arc melted and cast in a form of bar. It was subsequently HIPed at temperature 1250⁰C and at pressure around 176MPa for 4 hours to remove porosity and other casting defects.

3.1 Preparation of Starting Material

Small pieces of the sample was cut from the bar using an ISOMET Low Speed Saw. These samples were sealed in quartz tube in argon atmosphere (~ 1 Psi pressure). Pressure of argon atmosphere inside the tube was calculated using the gas law. The calculated pressure inside the tube at room temperature should be such that it does not exceed 1 atm. at 1400⁰C since the tube may burst if pressure inside the tube is higher than the outside pressure. Fusion temperature of quartz is near 1400⁰C and hence the capsules sealed in vacuum can collapse at 1400⁰C. Hence, vacuum sealing was not done for preparation of the starting material. The sealed samples were then homogenized at 1400⁰C for 4 hours and then ice water quenched to retain the structure obtained at that

temperature. These quenched samples were used as the starting material for further heat treatments. All the samples were sealed in quartz tube under high vacuum before further heat treatment.

3.2 Heat Treatments

To study the phase transformation modes occurring in the material, the samples were heat treated at different temperatures for different holding times and with different cooling rates. Various temperatures and times selected for the experiment are 850⁰C and 900⁰C for 140 hours, 1150⁰C for 48 hours, 1200⁰C for 24 hours and at 1320⁰C for 2 hours followed by furnace cooling, air cooling and water quenching.

3.3 Characterization of Samples

The heat treated samples were first ground on emery belt and then polished with standard emery paper. Final polishing was done on wheel polisher using fine alumina (~0.3 μ m) and ultrafine alumina (~0.05 μ m) suspensions. The polished samples were then subjected to various characterization techniques:

3.3.1 Scanning Electron Microscopy

JEOL JSM 840A Scanning Electron microscope was used for metallography. The polished samples were etched with 8% HNO₃ + 4%HF and rest water. SEM was used to

identify various phases present in the sample and to study change in structure with different heat treatments. For detailed study, magnification upto 5000X was used.

3.3.2 X-ray Diffraction

In order to identify the phases present in the sample and to verify the SEM results and to find the volume fraction of different phases, X-ray diffraction studies were carried out on Seifert ISO DEBYEFLEX 2002 diffractometer, which is fitted with a graphite monochromator using $\text{CuK}\alpha$ radiation. The diffraction data was standardized using pure silicon. All the diffraction patterns were obtained under identical conditions, as given below:

Voltage - 30KV
Current - 20mA
Scanning Speed - $3^\circ/\text{min}$ (in 2θ)
Chart Speed - 3cm/min
Time Constant - 10sec
Counts per sec - 5k

Identical conditions were maintained to compare the XRD pattern obtained for different samples. The relative intensities as obtained from the X-ray diffraction patterns were compared with the theoretically calculated values. The peaks obtained were also used to calculate the volume fraction of the phases.

3.3.3 Electron Probe Micro Analyser

For the analysis of composition variation within the sample and to find the atomic fraction of each element in different phases during different heat treatments, EPMA was done using Super Probe JXA-8600MX. The beam size used was approximately 2-3 μm in diameter.

3.4 Micro Hardness Test

Micro hardness test was performed using a Leitz Miniload microhardness tester using Vickers' scale on all the heat treated samples to understand the effect of heat treatment and consequently, effect of microstructure on the hardness of material. Micro hardness test produces square indentation with almost same diagonal length. The diagonal length was measured (in micrometer) at right angles, and the average of two readings was used to read the hardness value directly from the charts available. 4-5 readings were taken for each sample. Load used for the test was 100gm. Hardness value obtained has in kg/mm^2 .

CHAPTER 4

RESULTS AND DISCUSSION

4.1 Starting Material

The as received material has a coarse lamellar structure, shown in figure 4.1a. The bright region represents the α phase while dark region is the γ phase. α phase shows a complex structure at higher magnification with the dark γ phase nucleated within the bright phase (figure 4.1b).

The starting material for this work was produced by homogenization of the as-received material at 1400°C (single phase region) for 4 hours followed by ice water quenching. SEM micrograph of homogenized sample is given in figure 4.2a. The microstructure reveals large α grains of size approximately $150\text{--}400\mu\text{m}$ with slightly serrated grain boundaries.

Large grains are formed during holding of samples at high temperature for a long period of time. During quenching the γ phase starts nucleating within the α phase along some particular direction. Figure 4.2b shows serrated grain boundary in the homogenized sample at a higher magnification. Very high rate of cooling prevents complete

transformation of the coarse α grains to lamellar structure. Figure 4.2c shows the fine details of the structure. However it has been reported that fully lamellar structure forms when the sample is slowly cooled from 1400°C [15].

EPMA was used to determine the chemical composition of the ice water quenched sample. The smallest beam size that could be obtained in the EPMA was approximately 2-3 μ m while figure 4.2c clearly shows that the dimensions of the individual constituents is much smaller. Therefore, only the bulk composition could be obtained. The bulk composition obtained and the nominal composition in terms of atom percent is given below in table 4.1.

Table 4.1: EPMA result

	Ti(at %)	Al(at %)	Nb(at %)	Mn(at %)
EPMA result	50.3765	46.0570	2.0438	1.5227
Nominal composition	50	46	2	2

4.1.1 X-Ray Diffraction

X-ray diffraction patterns obtained for the starting material were found to be non-reproducible. Figure 4.3 shows the X-ray diffraction pattern of the sample in two different orientations. It can be clearly seen that orientation has strong effect on the intensities. This is because, during cooling, the α phase starts decomposing and γ starts nucleating within the α phase along a particular direction. The two phases have the following orientation relationship; $(0001)_{\alpha} // \{111\}_{\gamma}$ and $\langle 1120 \rangle_{\alpha} // \langle 110 \rangle_{\gamma}$ [5]. Table

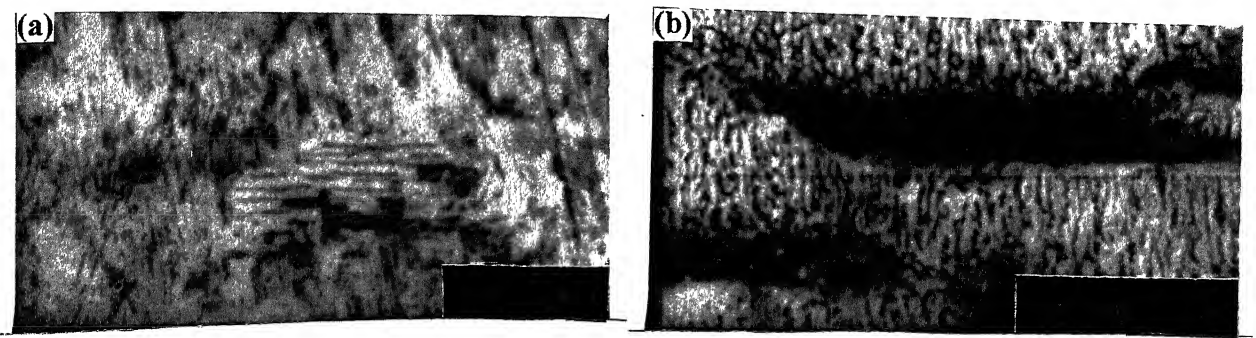


Figure 4.1: SEM micrographs of the as-received material at (a) 300X and (b) 5000X.

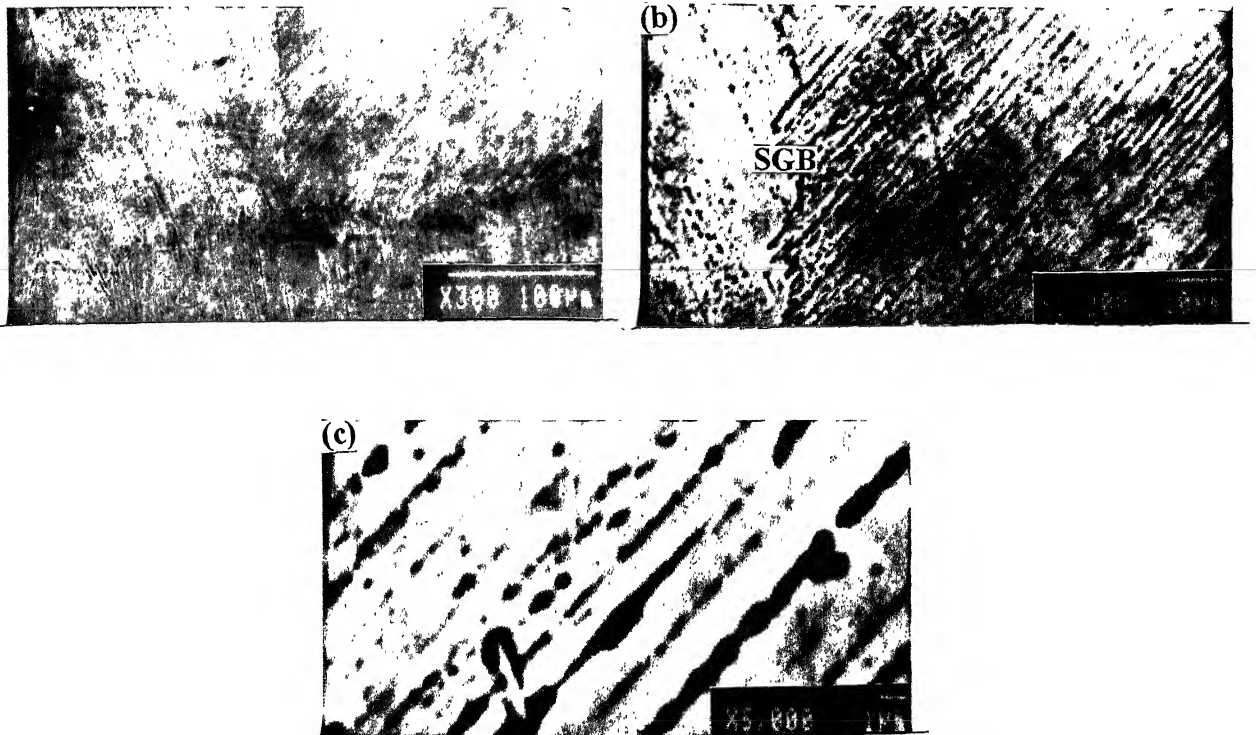


Figure 4.2: SEM micrographs of the starting material at, (a) 300X showing large grains, (b) 1200X showing serrated boundary and (c) 5000X showing fine details.

SGB represents serrated grain boundary.

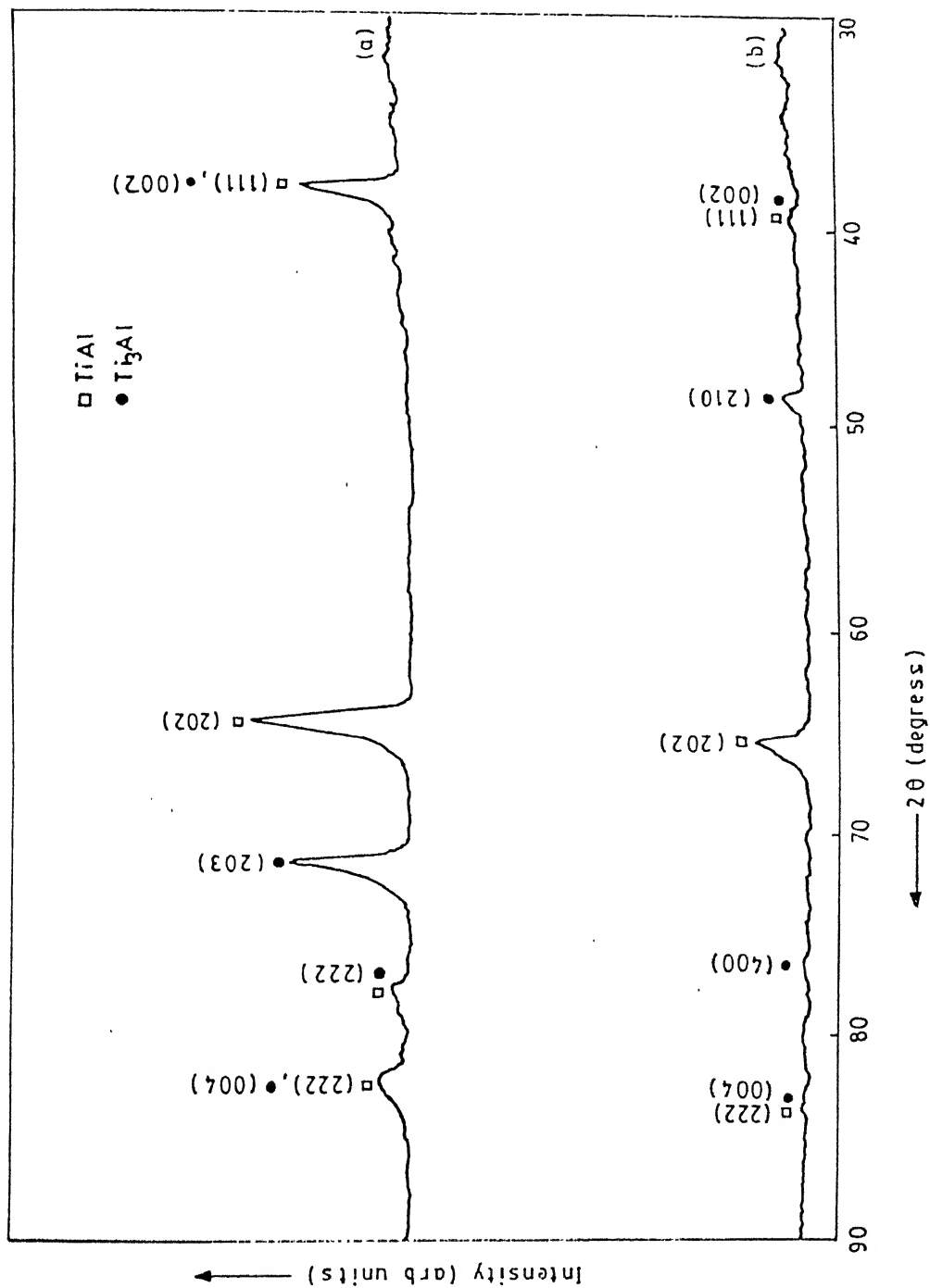


Figure 4.3: XRD patterns from the starting material in two different orientations.

4.1 gives the positions of some of the important peaks and their relative intensities as observed in the X-ray diffraction pattern obtained for the homogenized samples. This is attributed to the presence of extremely large grains and due to γ phase which is present along some particular crystallographic direction within the α grains (figure 4.2c). Due to this effect of orientation the X-ray results on the starting material were not used for any further analysis.

Table 4.1- Important peaks and their relative intensities for starting material.

S.No	2 θ (degrees),	(hkl)	(I/I _{max}) _a (From fig.4.3a)	(I/I _{max}) _b (From fig.4.3b)
1.	38.85	\square (111), \bullet (002)	46.67	13.42
2.	48.6	\bullet (210)	-	23.15
3.	65.6	\square (202)	100	100
4.	72.1	\bullet (203)	63.12	-
5.	76.6	\bullet (400)	-	8.05
6.	78.45		8.95	-
7.	83.6	\square (222), \bullet (004)	18.54	7.04

\square represents TiAl and \bullet represents Ti₃Al

4.2 Water Quenched Samples

4.2.1. Scanning Electron Microscopy

The homogenized samples were further heat treated by water quenching from different temperatures, 850⁰C, 900⁰C, 1150⁰C and 1320⁰C for different times. These temperatures were selected to study the effect of annealing temperatures on discontinuous coarsening, which is a transformation process by which the primary lamellar structure is modified. It has been reported by some researchers [6] that for most of the alloys, discontinuous coarsening (section 2.7.2) decreases with increasing temperatures, i.e, as the α -transus is reached, and more classical coarsening mode becomes operative. Transformation by discontinuous coarsening almost disappears below 900⁰C and it is maximum between 1100⁰C and 1200⁰C.

Figure 4.4 shows the SEM micrographs of the samples water quenched from different temperatures. After holding the sample at 850⁰C for 140hrs, a fully lamellar structure is evolved and γ phase is observed to nucleate at the boundaries of the lamellar colonies (figure 4.4a). The size of these colonies varies from 400-800 μ m while in starting structure the size was in the range 150-400 μ m. Water quenched samples from 900⁰C held for 140 hours show the γ phase growing within the lamellar colony (figure 4.4b) and it is also expected to grow at the grain boundaries. However, it could not be experimentally observed. Micrographs for the samples water quenched from 1150⁰C show lamellar colonies with wide range of shapes and size and also with varying plate thickness (figure

4.4c). Some part of the micrograph shows lamellar colonies with very smooth boundaries while in some regions the boundary between the lamellar colonies are highly serrated and they show interpenetrating grains. Smooth boundaries result from continuous coarsening while discontinuous coarsening leads to serrated boundaries. Hence it can be said that at 1150°C the initial lamellar structure gets modified by both continuous and discontinuous coarsening. As the annealing temperature is further increased to 1320°C, the discontinuous mode of coarsening is seen to dominate as shown in figure 4.4d. It is observed that the grain boundaries penetrate into each other, thus resulting into serrated boundaries. The lamellae also become coarse.

Due to the complexity and fineness of the structure quantitative metallography was not possible for any of the samples.

4.2.2. X-Ray Diffraction

For the calculation of theoretical value of the intensity from TiAl and Ti₃Al phases at various 2θ values, following well known relationship has been used.

$$I_{th} = \frac{1}{V^2} |F|^2 \cdot m \cdot LP \cdot e^{-2M}$$

Where,

I_{th} is the theoretically calculated intensity,

V is the volume of the unit cell,

For TiAl, $V = a^2c$; $a = 3.986 \text{ \AA}$, $c = 4.04539 \text{ \AA}$

For Ti₃Al, $V = 0.866 a^2c$; $a = 5.746 \text{ \AA}$, $c = 4.624 \text{ \AA}$

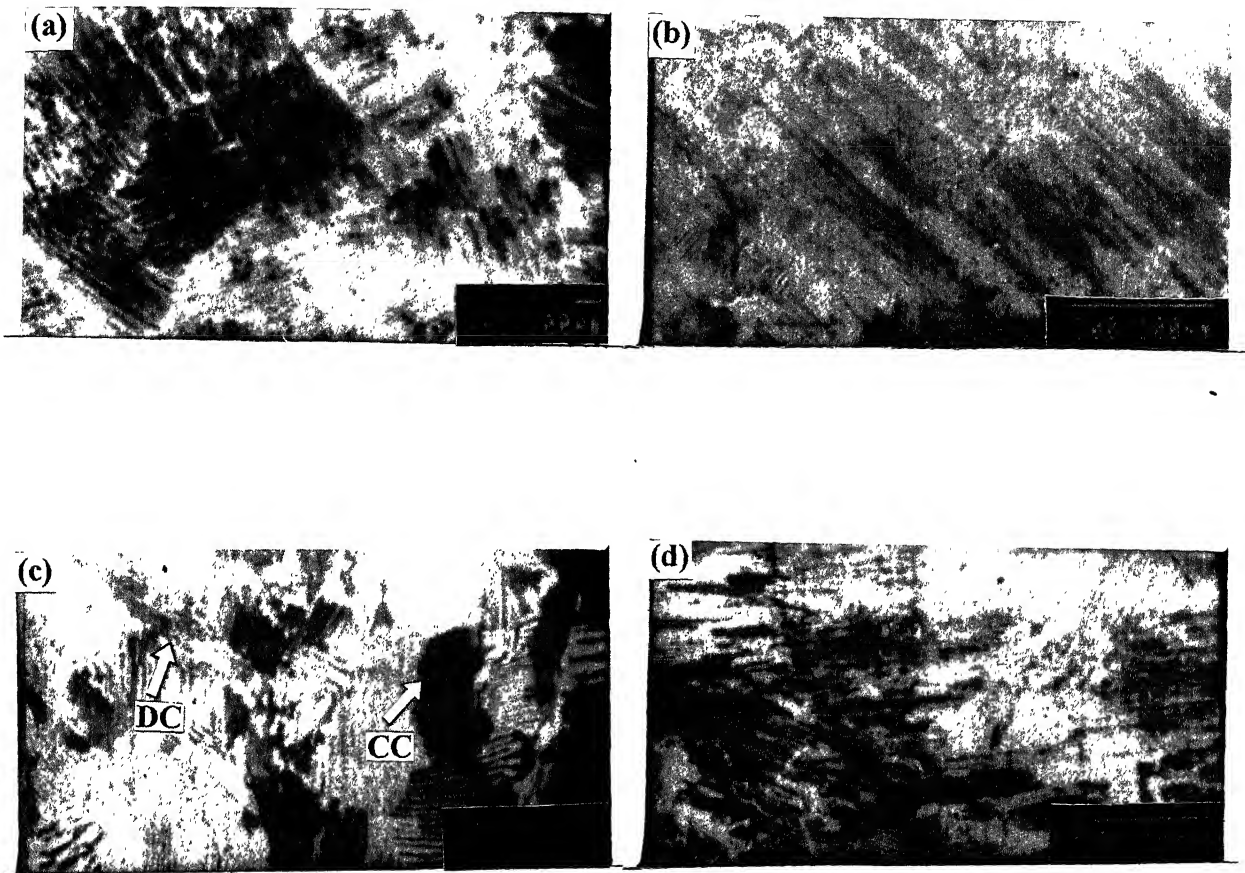


Figure 4.4: SEM micrographs of the water quenched samples from, (a) 850⁰C, (b) 900⁰C, (c) 1150⁰C and (d) 1320⁰C.

DC represents discontinuous coarsening and CC represents continuous coarsening

F is the structure factor. General formula of structure factor is given in appendix I. Atom position in the unit cell for both the phases is given in appendix I which is required for the derivation of the structure factor.

For TiAl,

$$|F|^2 = 16 [f_{Al} X_{Al} + f_{Ti} (1 - X_{Al})]^2$$

For Ti₃Al,

$$|F|^2 = 16 C [f_{Al} X_{Al} + f_{Ti} (1 - X_{Al})]^2$$

C = 4, h+2k = 3m, l is even,

C = 3, h+2k = 3m ± 1, l is odd,

C = 1, h+2k = 3m + 1, l is even.

f is the atomic scattering factor and X is the atomic fraction.

LP is the Lorentz-Polarisation factor;

$$LP = \frac{1 + \cos^2 2\theta}{\sin^2 \theta \cos \theta}$$

m is the multiplicity factor and it depends on the hkl value,

e^{-2M} is the temperature factor. It has not been considered for the calculation because of the unavailability of data.

Theoretically calculated intensity values for both the phases is given in appendix II.

Figure 4.5 shows the XRD patterns obtained from the water quenched samples. Most intense peak is obtained at 2θ equal to 38.9 for all the three samples. Maximum broadening is observed in the XRD pattern obtained from sample water quenched from

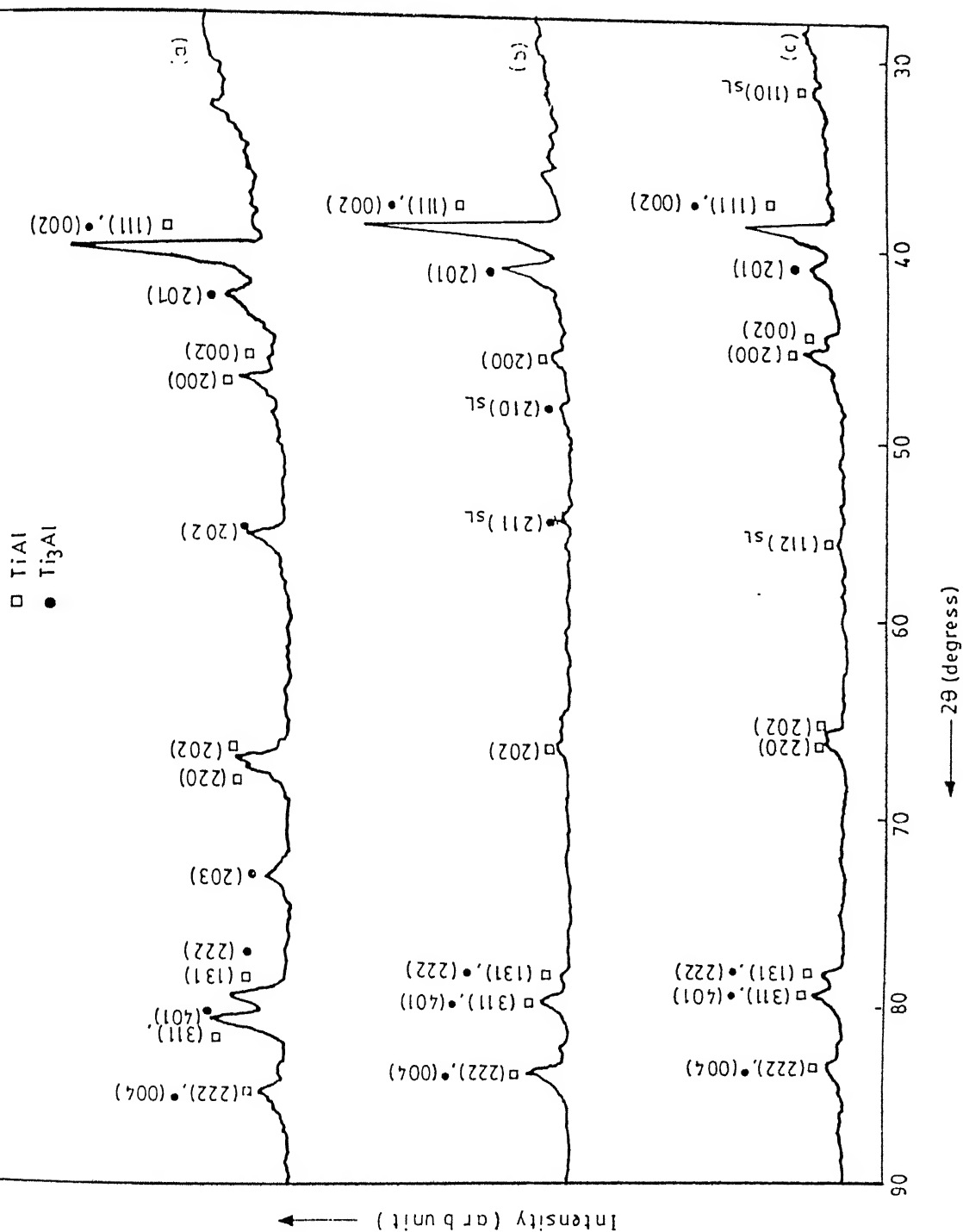


Figure 4.5: XRD patterns from the water quenched samples from, (a) 1320°C, (b)

1150°C, (c) 900°C.

900⁰C. Sample water quenched from 1320⁰C shows intense Ti₃Al peaks as compared to the other two samples. This is because at 1320⁰C, volume fraction of α phase much higher than the γ phase (table 4.4).

Patterns from the water quenched samples from 900⁰C and 1150⁰C show few superlattice peaks of very low intensity from both TiAl and Ti₃Al phases. However, due to extremely low integrated intensity, these peaks were not used for any further analysis. No superlattice peaks are observed for the sample quenched from 1320⁰C (figure 4.5a). Ordering of Ti₃Al, i.e, $\alpha \rightarrow \alpha_2$ transformation, occurs around 1180⁰C and hence no superlattice peak appears in the sample water quenched from 1320⁰C. Few peaks are present in sample water quenched from 1150⁰C (figure 4.5b) which means that ordering has occurred during holding of the sample. However, observed intensity is much smaller than the theoretically estimated value (refer appendix II), which may be due to partial ordering whereas complete ordering has been assumed in the calculations. Sample water quenched from 900⁰C do not show any superlattice peak from Ti₃Al phase that may be due to slower kinetics of $\alpha \rightarrow \alpha_2$ transformation at 900⁰C.

TiAl phase remains ordered upto its melting point and hence superlattice peaks for this phase is expected in all the three samples. However only the sample water quenched from 900⁰C show few TiAl superlattice peaks(figure 4.5c). This might be due to unfavourable thermodynamic and kinetic conditions at the other two temperatures and holding times.

Table 4.3 gives the positions of the important peaks observed in the water quenched samples. It also compares the relative intensity of the peaks as obtained from the XRD with the theoretically calculated relative intensities. However, these values show poor agreement especially at higher values of 2θ . The discrepancies in theoretical and observed values may be attributed to the following facts;

1. Broadening increases with increase in θ and errors in the measurement of integrated intensity of broad peaks is more as compared to the sharp peaks. Maximum discrepancy is observed for the composite peak at $2\theta = 78.1$ & 79.3 and $2\theta = 83.2$.
2. Stoichiometric composition has been assumed at all temperatures for calculation of theoretical intensity. However, both TiAl and Ti_3Al shows non stoichiometry which affects the intensity.
3. Temperature factor has not been considered for calculation. This factor has significant effect on intensity especially at higher value of 2θ . This is because high θ reflections involve of low d value and so u/d ratio increases, where u is the amplitude of the vibrating atom. Hence, effect of vibration is more at higher 2θ values.
4. Presence of mosaic structure increases the intensity of the diffracted beam and observed intensity is higher than the theoretically calculated values for such a structure. Mosaic structure is a crystal imperfection which is caused due to breaking of a single crystal.
5. At 1320°C discrepancy is very large for all values of 2θ . Due to extremely large grain size with plates of α and γ nucleated along a particular crystallographic direction, orientation of the sample significantly effects the integrated intensity as well as the

Table 4.3: Relative intensities of peaks for water quenched samples

S.No	2 θ	(hkl)	900 ⁰ C			1150 ⁰ C			1320 ⁰ C		
			Rel. Intensity			Rel. Intensity			Rel. Intensity		
			Theo	Obs.	%E	Theo.	Obs.	%E	Theo	Obs	%E
1.	38.7	$\square(111)$, $\bullet(002)$	100	100	0	100	100	0	43.6	100	129
2.	40.9;	$\bullet(201)$	28.3	36.5	28.9	41.44	33.8	-18	100	49.1	-50
3.	44.5, 45.4	$\square(200)$, $\square(002)$	44.1	56.4	27.8	31.96	6.8	-78	5.43	18.8	246
4.	65.4, 66.05	$\square(220)$, $\square(202)$	26.3	38.3	45.6	29.11	18.1	-38	3.33	35.4	963
5.	78.1, 79.3	$\square(311)$, $\bullet(401)$ $\square(131)$, $\bullet(222)$	38.5	65.7	70.6	40.37	26.3	-35	35.9	81.3	126
6.	83.25	$\square(222)$, $\bullet(004)$	9.39	27.5	192	10.63	26.0	144	4.11	16.3	296

\square represents TiAl phase and \bullet represents Ti₃Al phase

$$\%E = 100 \cdot (\text{obs} - \text{theo}) / \text{theo}$$

relative intensity of the peaks. This effect is observed to be very prominent in the sample water quenched from 1320°C.

The X-ray diffraction peaks were used to calculate the volume fraction of the two phases (TiAl and Ti₃Al) present in the alloy. The formula used for calculation is,

$$\frac{I_{\alpha}}{I_{\gamma}} = \frac{(I_{th})_{\alpha} C_{\alpha}}{(I_{th})_{\gamma} C_{\gamma}}$$

$$\text{and } C_{\alpha} + C_{\gamma} = 1$$

Where, I = integrated intensity of peaks in XRD pattern,

C = volume fraction of phases

I_{th} = theoretically calculated intensity.

Volume fraction obtained for both TiAl and Ti₃Al phases (V) in samples water quenched from 900°C, 1150°C and 1320°C is given in table 4.4. This table also compares the calculated values with the volume fraction measured from the phase diagram which is referred as V'. This volume fraction was calculated assuming the composition at the temperatures from where the samples were quenched.

Table 4.4: Volume Fraction of TiAl and Ti₃Al during different heat treatments (V is the volume fraction obtained from the XRD and V' from the phase diagram)

Annealing Temp.	Cooling	TiAl			Ti ₃ Al		
		V	V'	%error	V	V'	%error
1320 ⁰ C	Water Quenching	0.245	0.1667	+31.9	0.755	0.8333	-10.3
1150 ⁰ C	Water Quenching	0.7585	0.7391	+2.5	0.2414	0.2608	-8.0
900 ⁰ C	Water Quenching	0.7339	0.7894	-7.5	0.266	0.2105	+20.8
1150 ⁰ C	Furnace Cooling	0.8038	0.7857	+2.2	0.1961	0.2143	-9.2
900 ⁰ C	Furnace Cooling	0.7789	0.7857	-0.87	0.2211	0.2143	+3.0

$$\%error = 100.(V-V')/V'$$

Some discrepancy is observed in volume fractions calculated from the XRD and from phase diagram. This can be due to some transformation that may have occurred during quenching which has not been taken into account while calculating the volume fraction from the phase diagram. Some amount of error is also introduced during the measurement of integrated intensity of composite peaks that could not be resolved very accurately. Hence only few peaks at lower 2θ values have been used for the calculation since peaks become broader at higher 2θ and consequently more error is introduced.

4.3 Furnace Cooled Samples

4.3.1 Scanning Electron Microscopy

Furnace cooling from 900⁰C and 1150⁰C results in the evolution of similar type of structures. Figure 4.6 shows the SEM micrographs of the furnace cooled samples. Both the microstructures reveal network of α and γ phases. This type of structure is often referred to as monolithic γ grains or near γ structure[16,17]. It is characterized by a continuous network of γ phase. When furnace cooled from 900⁰C, very fine network of α phase is observed to have formed within the monolithic γ grain (figure 4.6a). However at higher temperature (1150⁰C), the α phase becomes coarser and assumes slightly equiaxed shape (figure 4.6c). This structure is clearer at higher magnification of the sample furnace cooled from 1150⁰C (figure 4.6d). Higher magnification shows dark phase nucleated within the bright phase. This type of structure is observed in all the samples at higher magnification. However, analysis of this complex structure within the bright phase requires detailed TEM study.

Furnace cooled samples do not show any discontinuous coarsening. Hence this mode of transformation is a strong function of cooling rate. It has been reported [17] that for two phase alloys (Al – 45 to 48%), nearly gamma type microstructure results when the material is subjected to long heating time and slow cooling form α and γ phase field. When the homogenized sample was furnace cooled from 1200⁰C after holding for 24 hours, the structure obtained is similar to that obtained after water quenching from 1150⁰C (figure 4.7), i.e, consisting of continuously and discontinuously coarsened

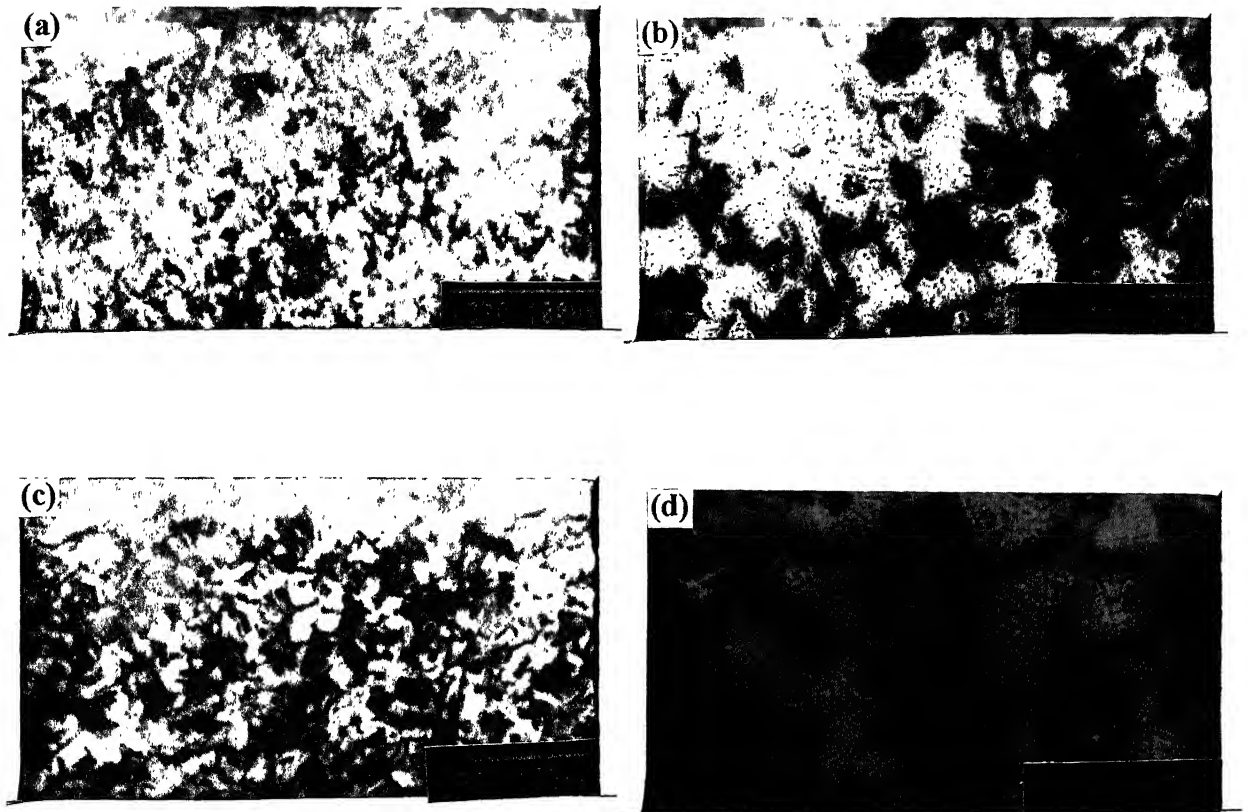


Figure 4.6: SEM micrographs of the furnace cooled samples at different magnifications from, (a) and (b) 900°C, (c) and (d) 1150°C.

lamellar colonies. It does not show formation of monolithic γ grains. There could be two possibilities for this transformation. Either the holding time of 24 hours is not sufficient for the formation of near γ structure or modification of primary lamellae by forming monolithic γ grains is retarded as the temperature is increased in $\alpha+\gamma$ phase fields. However confirmation of exact mechanism requires further work.

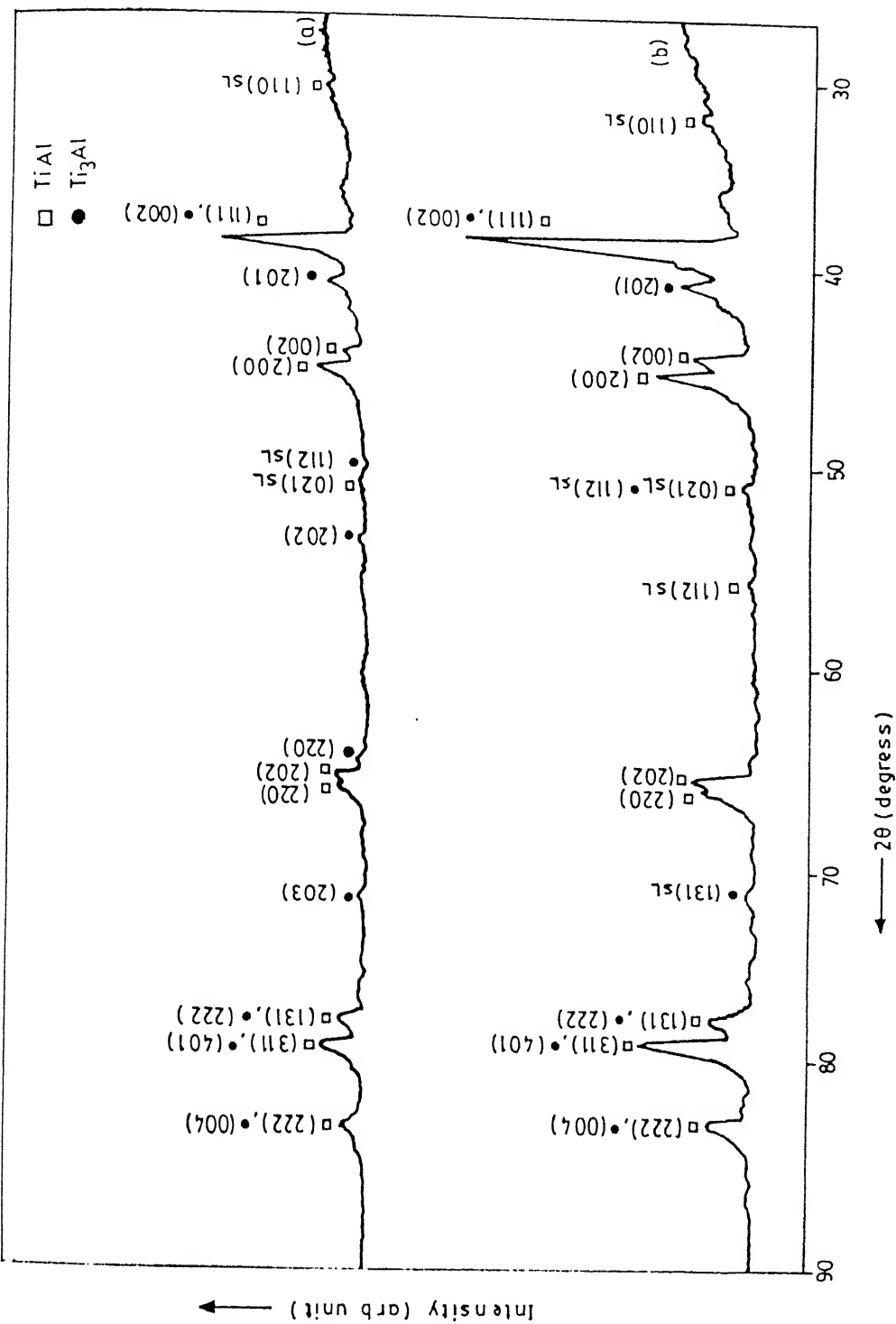


Figure 4.7: SEM micrograph of sample furnace cooled from 1200°C.

4.3.2 X-Ray Diffraction

Figure 4.7 shows the XRD patterns obtained for the furnace cooled samples. Highest intensity peak is obtained at 2θ equal to 38.9 for both the samples. The superlattice peaks appear in XRD from both the heat treatments for TiAl as well as Ti_3Al phase. Hence both the phases undergo ordering reaction upon slow cooling. However, the relative intensities of these peaks are extremely small as compared to the relative intensities of the fundamental peaks due to incomplete ordering. Hence they have not been considered for any further analysis. XRD charts show strong γ peaks at 2θ equal to 44.5 & 45.4 and 2θ equal to 65.4 & 66.0 which confirms the formation of monolithic γ grains or formation of near gamma structure.

Figure 4.8: XRD patterns from the samples furnace cooled from, (a) 1150°C and (b) 900°C.



Important peaks obtained for the furnace cooled samples are listed in table 4.5. The table also compares the relative intensities of the peaks obtained from the X-ray diffraction with the theoretically calculated values. At lower values of 2θ , these values show good agreement, however some discrepancy appears as the 2θ value increases. The reason for the discrepancy is explained in section 4.2.2. XRD pattern from the sample furnace cooled from 1200°C has not been used for analysis because of its non reproducibility.

Volume fractions for the furnace cooled samples were calculated using the same relationships as used for the water quenched samples. Volume fractions of the two phases as calculated from the XRD peaks and from the phase diagram are compared in table 4.4.

The observed and the theoretical values show good agreement. At 900°C , volume fraction of γ obtained from XRD is slightly less than the volume fraction calculated from phase diagram while it is slightly high for the sample furnace cooled from 1150°C . This discrepancy can be due to the assumptions made in the calculations or due to the approximations made in resolving the double peaks.

Table 4.5: Relative intensities of important peaks for furnace cooled samples.

S.No.	2 θ	(hkl)	900 $^{\circ}$ C			1150 $^{\circ}$ C		
			Rel. Intensity			Rel. Intensity		
			Theo.	Obs.	%error	Theo.	Obs.	%error
1.	38.7	$\square(111)$, $\bullet(002)$	100	100	0	100	100	0
2.	40.9	$\bullet(201)$	28.92	25.2	-12.8	28.92	27.6	-4.5
3.	44.5, 45.4	$\square(200)$ $\square(002)$	44.0	46.17	+4.9	44.0	46.7	+6.1
4.	65.4, 66.0	$\square(220)$ $\square(202)$	26.28	33.75	+28.4	26.28	40.78	+55.2
5.	78.1, 79.3	$\square(311)$, $\bullet(401)$ $\square(131)$, $\bullet(222)$	38.69	61.29	+58.4	38.69	84.56	+118.5
6.	83.25	$\square(222)$, $\bullet(004)$	9.39	18.54	+97.4	9.39	21.65	+130.5

\square represents TiAl phase and \bullet represents Ti_3Al phase.

$$\% \text{error} = 100.(\text{obs.} - \text{theo.})/\text{theo.}$$

4.4 Air Cooled Sample

Air cooling was done only from 1150°C . Figure 4.8 shows the SEM micrograph of the sample. The structure is similar to that obtained from the sample water quenched from 1150°C . But the size of lamellar colony is larger for the air cooled sample. It also shows few equiaxed γ grains. Due to extremely large grain size, orientation has significant effect on the integrated intensities of the peaks. Hence the X-ray diffraction result has not been used for any analysis.



Figure 4.9: SEM micrograph of the sample air cooled from 1150°C .

EQ represents equiaxed grain.

4.5 Microhardness Test

Micro hardness test was performed on all the samples and the results obtained are given in table 4.6. Hardness of water quenched samples from 1320°C , 1150°C and 900°C are 360, 370 and 468 H_v respectively. This can be attributed to lesser amount coarsening in

the sample water quenched from 900°C . Extent of Coarsening in sample water quenched from 1320°C and hence it shows lowest hardness value. For the furnace cooled samples, hardness values obtained are 376 and 317 H_v for samples from 900°C and 1150°C respectively. Hardness for samples from 1150°C is lower because at that temperature because the α phase is much coarser. It can be observed that the water quenched samples have higher hardness than the furnace cooled ones. This is because furnace cooling leads to monolithic γ structure which has lower hardness than the α phase. Hence it can be concluded that transformation of primary lamellae by the formation of monolithic grains causes deterioration in the hardness of the material. Air cooled sample from 1150°C shows hardness in between the hardness of furnace cooled and water quenched sample.

Table 4.6: Hardness variation for different heat treatments

Annealing Temperature	Cooling	Hardness, H_v
900°C	Water Quenching	468
900°C	Furnace Cooling	376
1150°C	Water Quenching	370
1150°C	Air Cooling	351
1150°C	Furnace Cooling	317
1320°C	Water Quenching	360

CHAPTER 5

CONCLUSIONS

1. Fully lamellar structure is obtained after holding the sample at 850°C for 140 hours.
2. Coarsening of lamellar structure begins at 900°C with γ phase precipitating from the primary lamellae and at the grain boundaries.
3. At 1150°C , modification of primary lamellar structure occurs by both continuous and discontinuous coarsening.
4. As the α -transus is approached, extent of discontinuous coarsening increases.
5. Furnace cooling from both 900°C and 1150°C results in modification of initial structure by formation of monolithic γ grains.
6. Decreasing the holding time prevents formation of monolithic γ grains hence this transformation is a strong function of holding time and cooling rate.
7. Formation of monolithic γ grains and discontinuous coarsening of primary lamellae results in decrease of hardness. Monolithic γ grains have lower hardness values than the discontinuously coarsened lamellar structure.
8. Samples, both water quenched and furnace cooled from 900°C and 1150°C show superlattice peaks hence ordering takes place both during holding the samples and during cooling from below the ordering temperature.

9. Since quantitative metallography is not possible for any of the samples because of the complexity of structures in all the samples, volume fractions obtained from x-ray diffraction data can be reliably used for analysis.

Suggestions for Future Work

Due to some limitations, very few heat treatments were done. However, in order to develop a better understanding of coarsening behaviour, further heat treatments are required at high temperatures in $\alpha+\gamma$ phase field. To study the ordering reaction in both TiAl and Ti₃Al phases, annealing for longer time should be done and slower cooling rates should be adopted in order to achieve complete ordering.

TEM analysis is required to resolve the complex structure within the α phase, observed in micrographs of all the samples at higher magnification.

REFERENCES

1. C.McCullough, J.J.Valencia, C.G.Levi and R.Mehrabian, *Acta mater.*, Vol.37, No.5, (1989), P 1321-1336.
2. Y.I.Kematsu, T.Hanamura, H.Morikawa, M.Tanino and J.Takamura, *Intermetallic compounds-structure and mechanical properties*, ed. O.Izumi, The Jpn. Inst. Met., (1991), P 191.
3. K.Kasahara, K.Hachimoto, H.Doi and T.T.Sujimoto, *J. Jpn. Inst. Met.*, Vol 53, (1990), P 58.
4. F.H.Froes, C. Suryanarayana and D.Eliezer, *Journal of Mat. Sc.*, Vol.27, (1992), P 5113-5140.
5. A.Denquin and S.Naka, *Acta Mater*, Vol.44, No.1,(1996), P343-352.
6. A.Denquin and S.Naka, *Acta mater.*, Vol.44, No.1, (1996), P 353-365.
7. X.D.Zhang, S.Godfrey, M.Weaver, M.Strangwood, P.Threadgill, M.J.Kaufman and M.H.Loretto, *Acta Mater.*, Vol.44, No.9, (1996), P 3723-3734.
8. S.A.Jones and M.J.Kaufman, *Acta metall. Mater.*, Vol.41, No.2, (1993), P 387-398.
9. X.D.Zhang, T.A.Dean and M.H.Loretto, *Acta metall. Mater.*, Vol.42, No.6, (1994), P2035-2042.
10. Y.W.Kim, *Acta Metall. Mater.*, Vol.40, (1992), P1121.
11. Y.W.Kim, *JOM*, July(1994), P 30-39.
12. Helmet Clemens, *Z.Metallkd.*, Vol.86, No. 12, (1995), P 814.

13. D.S.Shih, Microstructure /property relationship in titanium aluminides and alloys, eds. Y.W.Kim and R.R.Boyer TMS (1990).
14. D.S.Schwartz and W.O.Soboyejo, Microstructure /property relationship in titanium aluminides and alloys, eds. Y.W.Kim and R.R.Boyer TMS (1990).
15. Y.G.Li and M.H.Loretto, *Acta Metall. Mater.*, Vol. 42, No.6, (1994), P 2009-2017.
16. A.Denquin, S.Naka and T.Khan, Titanium '92, science and Technology,(ed. By F.H.Froes and I.L.Caplan) TMS Warrendale, Pa (1992), P1017.
17. A.Denquin and S.Naka, *J. Phys. III*, Colloque C7 3, (1993), P 383.
18. R.V.Ramanujan, *Acta metall. Mater.*, Vol.42, No.7, (1994), P 2313-2322.
19. H.M.Flower and J.Christodoulo, *Mat. Sc. & Tech*, Vol.15, (1999), P 45-51.
20. R.V.Ramanujan, *Acta metall mater*, Vol.42, No.8,(1994), P 2775-2781.
21. R.V.Ramanujan, *Acta mater*, Vol.44, No.7, (1996), P 2611-2642.
22. S.Sen and D.M.Stefanescu, *JOM*, May(1991), P 30-34.
23. Y.W.Kim, *JOM*, July(1989), P 24-30.
24. Y.W.Kim, *JOM*, July(1995), P 38-41.
25. D.S.Shong and Y.W.Kim, *Scripta met.*, Vol.23,(1989), P 257-261.
26. D.Vujic, Zhixian Li and S.W,Whang, *Met. Trans. A*, Vol.19A, Oct(1988), P 2445-2455.
27. R.V.Ramanujan, *Acta Metall. Mater.*, Vol.43, No.12, (1995), P 4439-4451.
28. R.V.Ramanujan and P.J.Maziasz, *Metall. & Mater. Trans. A*, Vol.27A, June(1996), P 1661-1673.
29. S.L.Semiatin and P.A.McQuay, *Metall. Trans A*, Vol.23A, Jan.(1992)P 149-161.

30. S.Swaminathan, I.P.Jones, N.J.Zaluzec, D.M.Maher and H.L.Fraser, *Mat. Sc. & Engg.* A170, (1993), P 227-235.
31. H.J.Klaar, F.Y.Iisu, G.X.Wang and M.Dahms, *Z.Metallkd.*, Vol.85, No.12, (1994), P 863-866.
32. E.A.Ott and T.M.Pollock, *metall & Mater.Trans A.*, Vol.29A, March (1998), P 965-978.
33. M.A.Grinfeld, P.M.Hazzledine, B.Shoykhet and D.M.Dimiduk, *Metall. & Mater. Trans A*, Vol.29A, March (1998), P 937-942.
34. Y.Umakoshi, H.Y.Yasuda, T.Nakano and K.Ikeda, , *Metall. & Mater. Trans A*, Vol.29A, March (1998), P 943-950.
35. J.Panova and D.Farkas, , *Metall. & Mater. Trans A*, Vol.29A, March (1998), P 951-955.
36. T.S.Rong, I.P.Jones and R.E.Smallman, *Acta Mater.*, Vol.46, No.13, (1998), P 4507-4517.
37. D.Hu, A.Godfrey, P.A.Blenkinsop and M.H.Loretto, *Metall. & Mater. Trans.A*, Vol.29, March (1998), P 919-925.
38. G.W.Qin and Shi-Ming Hao, *Scripta Mater.*, Vol.37, No.7, (1997), P 937-942.
39. R.G.Rowe and S.C.Huang, *Israel Journal of Tech.*, Vol.24, (1998), P 255-260.
40. P.Bartolotta, J.Barret, J.Kelly and R.Smashey, *JOM*, May (1997), P 48-50

APPENDIX I

The general expression for the structure factor, F , is given by the well known relationship,

$$F = \sum f_n \exp 2\pi i (hu_n + kv_n + lw_n)$$

Where, u_n , v_n and w_n are the locations of the n th atom in the unit cell and f_n is the atomic scattering factor of the n th atom and h, k, l are the indices of the reflecting plane.

It can be seen from fig 2.2b that unit cell of TiAl consists of 2 Ti and 2 Al atoms located at the following positions:

$$\text{Al} - (0,0,0) \text{ and } (1/2, 1/2, 0)$$

$$\text{Ti} - (1/2, 0, 1/2) \text{ and } (0, 1/2, 1/2)$$

From figure 2.2a, it can be seen that 2Al and 6 Ti atoms are present in the unit cell of Ti_3Al at the following positions:

$$\text{Al} - (0,0,0) \text{ and } (1/3, 2/3, 1/2)$$

$$\text{Ti} - (1/2, 0, 0), (0, 1/2, 0), (1/2, 1/2, 0), (1/3, 1/6, 1/2), (5/6, 1/6, 1/2) \text{ and } (5/6, 2/3, 1/2)$$

Substituting the atom positions in the above equation gives the structure factor for TiAl and Ti_3Al .

APPENDIX II

Table showing theoretically calculated intensity for TiAl

S.No.	(hkl)	θ	m	LP	$ F ^2$	I_{th}
1.	(111)	19.45	8	15.34	2342.31	69.61
2.	(002)	22.38	2	11.21	2100.7	11.4
3.	(200)	22.73	4	10.82	2073.7	21.74
4.	(202)	32.85	8	4.72	1454.7	13.31
5.	(220)	33.13	4	4.64	1441.6	6.48
6.	(131)	39.79	16	3.28	1169.0	14.85
7.	(311)	39.28	8	3.34	1186.9	7.69
8.	(222)	41.77	8	3.05	1103.2	6.53
9.	(110) _{SL}	15.86	4	23.98	180.55	4.19
10.	(112) _{SL}	27.95	8	6.77	115.95	1.52
11.	(021) _{SL}	25.52	8	8.32	125.93	2.03

Table showing theoretically calculated intensities for Ti_3Al

S.No.	(hkl)	2θ	m	LP	$ F ^2$	I_{th}
1.	(002)	19.46	2	15.33	11949.97	20.97
2.	(201)	20.58	12	13.54	8594.0	79.88
3.	(202)	27.05	12	7.29	2265.5	11.34
4.	(203)	36.00	12	3.91	5044.6	13.56
5.	(222)	39.14	12	3.36	6113.0	14.13
6.	(401)	39.88	12	3.26	4486.6	10.07
7.	(004)	41.78	2	3.05	5663.7	1.98
8.	(210) _{SL}	21.55	12	12.21	36.29	0.30
9.	(211) _{SL}	26.23	24	7.81	92.13	0.98
10.	(112) _{SL}	25.31	12	8.48	126.8	0.73
11.	(131) _{SL}	35.62	24	4.00	68.74	0.37